ELSEVIER

International Journal of Solids and Structures 41 (2004) 5313–5325

INTERNATIONAL JOURNAL OF SOLIDS and STRUCTURES

www.elsevier.com/locate/ijsolstr

Modeling of monotonic and cyclic Swift effect using anisotropic finite viscoplasticity theory based on overstress (AFVBO): Part II—Numerical experiments

Ozgen U. Colak *

Mechanics of Materials Laboratory, Rensselaer Polytechnic Institute, Troy, NY 12180-3590, USA

Received 30 June 2003; received in revised form 23 February 2004
Available online 20 May 2004

Abstract

Anisotropic finite VBO given in Part I is used to model monotonic and cyclic Swift effects. The simulations were performed for fixed and deformation induced anisotropy. In the case of fixed anisotropy, it is assumed that the material is orthotropic. Material investigated at the fixed anisotropy is rolled copper. In the case of deformation induced anisotropy, the behavior of 70:30 brass under free-end torsion is investigated. The material is chosen as isotropic in the beginning of the deformation and allowed to evolve under large shear deformation. The simulation results are compared with experimental data obtained by Swift [Engineering 163 (1947) 253]. The Jaumann rate and the logarithmic rate are chosen as objective rates in the simulations. It is shown that anisotropic finite VBO can reproduce the monotonic and cyclic Swift effect quantitatively.

Keywords: Anisotropy; Swift effect; Free-end torsion; Viscoplasticity

1. Introduction

Axial length changes observed under free-end torsion of tubular or solid specimens are called the Swift effect, named after Swift (1947). Experiments, see Swift (1947), Billington (1976), Montheillet et al. (1985) and Wu et al. (1998), have shown that axial elongation induced under free-end torsion and axial stress build up under fixed end torsion result from deformation induced anisotropy. Therefore, in the constitutive model development, free-end and fixed end torsion tests have been used extensively to investigate modeling capability of the anisotropic models, Lowe and Lipkin (1991), Kuroda (1997, 1999), Krempl (1994), Majors and Krempl (1994) and Van der Giessen et al. (1992) just named a few.

* Present address: Yildiz Technical University, Istanbul, Turkey.
E-mail address: colako@alum.rpi.edu (O.U. Colak).

0020-7683/$ - see front matter © 2004 Elsevier Ltd. All rights reserved.
doi:10.1016/j.ijsolstr.2004.04.014

In Part I, isotropic finite viscoplasticity theory based on overstress is extended to anisotropy by introducing an anisotropic flow law with a fourth order inelastic compliance tensor. Inelastic compliance tensor is allowed to evolve during inelastic deformation.

In this paper, Part II, the modeling capability of anisotropic finite VBO has been investigated for free-end torsion. The evolution equations of anisotropic FVBO is given in Box I.

Box I. Anisotropic finite viscoplasticity theory based on overstress

The anisotropic flow law

$$\mathbf{D} = \mathbf{D}^e + \mathbf{D}^{\text{in}}, \quad \mathbf{D}^{\text{in}} = \frac{\overline{D}^{\text{in}}}{\Gamma}\mathbb{R} : \mathbf{O}, \quad \mathbf{O} = \boldsymbol{\sigma} - \mathbf{G}$$

Evolution equation for inelastic compliance tensor, $\mathbb{R}$

$$\mathring{\mathbb{R}} = \overline{D}^{\text{in}} b[\bar{e}](\mathbb{R} - \mathbb{T}), \quad \mathbb{T} = (\mathbb{R}_{\text{o}} : \boldsymbol{\chi}) \otimes (\mathbb{R}_{\text{o}} : \boldsymbol{\chi}), \quad \boldsymbol{\chi} = \frac{1}{\Gamma}\mathbb{R} : \mathbf{O}$$

$$\mathring{\mathbb{R}}_{ijkl} = \dot{\mathbb{R}}_{ijkl} + \mathbb{R}_{mjkl}\boldsymbol{\Omega}_{mi} + \mathbb{R}_{imkl}\boldsymbol{\Omega}_{mj} + \mathbb{R}_{ijml}\boldsymbol{\Omega}_{mk} + \mathbb{R}_{ijkm}\boldsymbol{\Omega}_{ml}$$

Incompressibility condition,

$$\mathbb{R}_{iikl} = \mathbb{R}_{klii} = 0$$

Hypoelastic relation between Cauchy stress rate and rate of deformation tensor

$$\mathbf{D}^e = \frac{\mathrm{D}}{\mathrm{D}t}(\mathbb{S}\boldsymbol{\sigma}), \quad \mathring{\boldsymbol{\sigma}} = \dot{\boldsymbol{\sigma}} + \boldsymbol{\sigma}\boldsymbol{\Omega} - \boldsymbol{\Omega}\boldsymbol{\sigma}$$

The evolution equation for the equilibrium stress

$$\mathring{\mathbf{G}} = \frac{\Psi[\Gamma]}{E}\left(\mathring{\boldsymbol{\sigma}} + \frac{\boldsymbol{\sigma} - \mathbf{G}}{k[\Gamma]} - \frac{\Gamma}{k[\Gamma]}\left(\frac{\mathbf{G} - \mathbf{K}}{A + \beta\Gamma}\right)\right) + \left(1 - \frac{\Psi[\Gamma]}{E}\right)\mathring{\mathbf{K}}$$

The evolution equation for the kinematic stress

$$\mathring{\mathbf{K}} = \frac{E_{\text{t}}}{k[\Gamma]}(\boldsymbol{\sigma} - \mathbf{G})$$

The isotropic stress

$$\dot{A} = A_{\text{c}}(A_{\text{f}} - A)\overline{D}^{\text{in}}$$

Invariants:

$$\overline{D}^{\text{in}} = \frac{\Gamma}{K_{\text{o}}k[\Gamma]}, \quad \Gamma = \sqrt{(\mathbb{R} : \mathbf{O}) : (\mathbb{R} : \mathbf{O})}$$

The theory is applied to free-end torsion using the logarithmic and the Jaumann stress rates. To this end the coupled, nonlinear, first order, ordinary differential equations are numerically integrated in the simulation of the test conditions reported by Swift (1947). The FVBO theory with fixed anisotropy as well as the initially isotropic FVBO but changing to an anisotropic theory can represent the monotonic and the cyclic Swift effect.

2. Numerical results

2.1. Kinematics

The free-end torsion problem, which will be analyzed here, is shown in Fig. 1. A thin walled tube subjected to free-end torsion has the following deformation, Zidi (2000).

$$r = r(R), \quad \theta = \Theta + \omega Z, \quad z = eZ \tag{1}$$

where (R, Θ, Z) and (r, θ, z) are initial (undeformed) and current (deformed) positions of a particle in cylindrical coordinate system, where ω is the twist angle per unit undeformed length.

Deformation gradient tensor, $\mathbf{F}$:

$$\mathbf{F} = \begin{bmatrix} \frac{\partial r}{\partial R} & \frac{1}{R}\frac{\partial r}{\partial \Theta} & \frac{\partial r}{\partial Z} \\ r\frac{\partial \theta}{\partial R} & \frac{r}{R}\frac{\partial \theta}{\partial \Theta} & r\frac{\partial \theta}{\partial Z} \\ \frac{\partial z}{\partial R} & \frac{1}{R}\frac{\partial z}{\partial \Theta} & \frac{\partial z}{\partial Z} \end{bmatrix} = \begin{bmatrix} \frac{\partial r}{\partial R} & 0 & 0 \\ 0 & \frac{r}{R} & \omega r \\ 0 & 0 & e \end{bmatrix} \tag{2}$$

The velocity gradient tensor, $\mathbf{L} = \dot{\mathbf{F}}\mathbf{F}^{-1}$, is obtained as follows:

$$\mathbf{L} = \begin{bmatrix} \frac{\partial \dot{r}}{\partial r} & 0 & 0 \\ 0 & \frac{\dot{r}}{r} & \frac{\dot{\omega} r}{e} \\ 0 & 0 & \frac{\dot{e}}{e} \end{bmatrix} \tag{3}$$

The rate of deformation tensor $\mathbf{D}$, which is symmetric part of velocity gradient tensor, $\mathbf{L}$ and the spin tensor, $\mathbf{W}$ the skew part of $\mathbf{L}$, are:

$$\mathbf{D} = \frac{1}{2}(\mathbf{L} + \mathbf{L}^{\mathrm{T}}) = \begin{bmatrix} \frac{\partial \dot{r}}{\partial r} & 0 & 0 \\ 0 & \frac{\dot{r}}{r} & \frac{\dot{\omega} r}{2e} \\ 0 & \frac{\dot{\omega} r}{2e} & \frac{\dot{e}}{e} \end{bmatrix} \tag{4}$$

$$\mathbf{W} = \frac{1}{2}(\mathbf{L} - \mathbf{L}^{\mathrm{T}}) = \begin{bmatrix} 0 & 0 & 0 \\ 0 & 0 & \frac{\dot{\omega} r}{2e} \\ 0 & -\frac{\dot{\omega} r}{2e} & 0 \end{bmatrix} \tag{5}$$

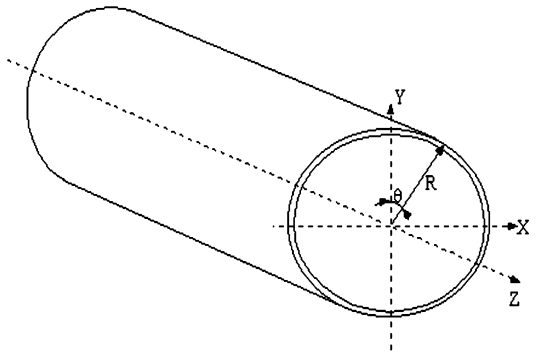

Fig. 1. Free-end torsion of a thin-walled tubular specimen.

2.2. Stresses and objectivity

Two corotational objective rates, which are the logarithmic rate, the Jaumann rate are employed in the analyses. An objective rate of the Cauchy stress is defined as

$$\mathring{\boldsymbol{\sigma}} = \dot{\boldsymbol{\sigma}} + \boldsymbol{\sigma}\boldsymbol{\Omega} - \boldsymbol{\Omega}\boldsymbol{\sigma} \tag{6}$$

where $\boldsymbol{\Omega}$ is a suitable skew-symmetric spin tensor. The Jaumann rate is obtained by replacing $\boldsymbol{\Omega}$ with the plastic spin $\mathbf{W}$.

Recently, Xiao et al. (1997) proved that the logarithmic rate of the Eulerian logarithmic strain measure, $\ln\mathbf{V}$, is equal to the rate of deformation tensor, $\mathbf{D}$. Among the co-rotational rates, this pair is the only one that has this property. They introduced a new spin tensor called logarithmic spin, or simply log spin. The logarithmic spin tensor $\boldsymbol{\Omega} = \boldsymbol{\Omega}^{\log}$ is given by

$$\boldsymbol{\Omega}^{\log} = \mathbf{W} + \mathbf{N}^{\log} \tag{7}$$

and

$$\mathbf{N}^{\log} = \begin{cases} 0, & b_1 = b_2 = b_3 \\ v[\mathbf{BD}], & b_1 \neq b_2 = b_3 \\ v_1[\mathbf{BD}] + v_2[\mathbf{B}^2\mathbf{D}] + v_3[\mathbf{B}^2\mathbf{DB}], & b_1 \neq b_2 \neq b_3 \end{cases} \tag{8}$$

where

$$v = \frac{1}{b_1 - b_2}\left(\frac{1 + (b_1/b_2)}{1 - (b_1/b_2)} + \frac{2}{\ln(b_1/b_2)}\right) \tag{9}$$

and b_i are the eigenvalues of left Cauchy–Green tensor $\mathbf{B} = \mathbf{F}\mathbf{F}^{\mathrm{T}}$.

$$v_k = -\frac{1}{\Delta}\sum_{i=1}^{3}(-b_i)^{3-k}\left(\frac{1+\varepsilon_i}{1-\varepsilon_i} + \frac{2}{\ln\varepsilon_i}\right), \quad k = 1,2,3 \tag{10}$$

$$\varepsilon_1 = b_2/b_3, \quad \varepsilon_2 = b_3/b_1, \quad \varepsilon_3 = b_1/b_2 \tag{11}$$

$$\Delta = (b_1 - b_2)(b_2 - b_3)(b_3 - b_1) \tag{12}$$

The following notation is used:

$$\begin{aligned} &[\mathbf{B}^r\mathbf{D}\mathbf{B}^s] = \mathbf{B}^r\mathbf{D}\mathbf{B}^s - \mathbf{B}^s\mathbf{D}\mathbf{B}^r, \quad [\mathbf{B}^r\mathbf{D}] = \mathbf{B}^r\mathbf{D} - \mathbf{D}\mathbf{B}^r \\ &[\mathbf{BD}] = \mathbf{BD} - \mathbf{DB}, \quad r,s = 0,1,2 \end{aligned} \tag{13}$$

The Cauchy stress tensor under free-end torsion is given as follows,

$$[\boldsymbol{\sigma}]_{r\theta z} = \begin{bmatrix} 0 & 0 & 0 \\ 0 & 0 & \sigma_{\theta z} \\ 0 & \sigma_{\theta z} & 0 \end{bmatrix} \tag{14}$$

To satisfy stress boundary conditions at rest, the equilibrium and kinematic stress tensors should have the same non-zero components as the Cauchy stress tensor.

$$\mathbf{G} = \begin{bmatrix} 0 & 0 & 0 \\ 0 & 0 & G_{\theta z} \\ 0 & G_{\theta z} & 0 \end{bmatrix}, \quad \mathbf{K} = \begin{bmatrix} 0 & 0 & 0 \\ 0 & 0 & K_{\theta z} \\ 0 & K_{\theta z} & 0 \end{bmatrix} \tag{15}$$

The simulations were performed for fixed anisotropy and deformation induced anisotropy. In the case of fixed anisotropy, it is assumed that the material is orthotropic. Material investigated at the fixed anisotropy

is rolled copper. In the case of deformation induced anisotropy, the behavior of 70:30 brass is investigated. The material is chosen as isotropic in the beginning of the deformation and allowed to evolve under large shear deformation. The simulation results are compared with experimental data obtained by Swift (1947). The Jaumann rate and the logarithmic rate, see Xiao et al. (1997), are chosen as the objective rates.

2.3. Fixed anisotropy

Constant inelastic compliance tensor, $\mathbb{R}$ is used for simulating fixed anisotropy. It is assumed that material is orthotropic. The orthotropic materials have mechanical properties that are different in three mutually perpendicular directions. They have three mutually perpendicular planes of material symmetry. In this case, the number of independent elastic constants is reduced to 9. Elastic compliance tensor, $\mathbb{C}$ in the six-dimensional space, see Lai et al. (1993), can be written as,

$$\mathbb{C} = \begin{bmatrix} \mathbb{C}_{11} & \mathbb{C}_{12} & \mathbb{C}_{13} & 0 & 0 & 0 \\ \mathbb{C}_{12} & \mathbb{C}_{22} & \mathbb{C}_{23} & 0 & 0 & 0 \\ \mathbb{C}_{13} & \mathbb{C}_{23} & \mathbb{C}_{33} & 0 & 0 & 0 \\ 0 & 0 & 0 & 2\mathbb{C}_{44} & 0 & 0 \\ 0 & 0 & 0 & 0 & 2\mathbb{C}_{55} & 0 \\ 0 & 0 & 0 & 0 & 0 & 2\mathbb{C}_{66} \end{bmatrix} \tag{16}$$

The inverse of $\mathbb{C}$ can be defined in terms of the engineering constants as follows, Lai et al. (1993)

$$\mathbb{C}^{-1} = \begin{bmatrix} \frac{1}{E_{11}} & \frac{-\nu_{12}}{E_{11}} & \frac{-\nu_{13}}{E_{11}} & 0 & 0 & 0 \\ \frac{-\nu_{12}}{E_{11}} & \frac{1}{E_{22}} & \frac{-\nu_{23}}{E_{22}} & 0 & 0 & 0 \\ \frac{-\nu_{13}}{E_{11}} & \frac{-\nu_{23}}{E_{22}} & \frac{1}{E_{33}} & 0 & 0 & 0 \\ 0 & 0 & 0 & \frac{1}{2\mu_{23}} & 0 & 0 \\ 0 & 0 & 0 & 0 & \frac{1}{2\mu_{13}} & 0 \\ 0 & 0 & 0 & 0 & 0 & \frac{1}{2\mu_{12}} \end{bmatrix} \tag{17}$$

where E_{11}, E_{22} and E_{33} are Young moduli, ν_{12}, ν_{13} and ν_{23} are the Poisson's ratios and μ_{12}, μ_{13} and μ_{23} are the shear moduli. The inelastic compliance tensor, $\mathbb{R}$ can be written in the six-dimensional space as follows,

$$\mathbb{R} = K_{\mathrm{o}} \begin{bmatrix} \frac{1}{K_{11}} & \frac{-\eta_{12}}{K_{11}} & \frac{-\eta_{13}}{K_{11}} & 0 & 0 & 0 \\ \frac{-\eta_{12}}{K_{11}} & \frac{1}{K_{22}} & \frac{-\eta_{23}}{K_{22}} & 0 & 0 & 0 \\ \frac{-\eta_{13}}{K_{11}} & \frac{-\eta_{23}}{K_{22}} & \frac{1}{K_{33}} & 0 & 0 & 0 \\ 0 & 0 & 0 & \frac{1}{2K_{23}} & 0 & 0 \\ 0 & 0 & 0 & 0 & \frac{1}{2K_{13}} & 0 \\ 0 & 0 & 0 & 0 & 0 & \frac{1}{2K_{12}} \end{bmatrix} \tag{18}$$

where K_{o} and K_{ij} are viscosity factors with the dimension of stress. η_{12}, η_{13} and η_{23} are the inelastic Poisson's ratios without dimension.

The behavior of rolled copper under free-end torsion is investigated. Elastic constants of copper are obtained from Tome (1998). The following assumption is made to calculate the inelastic Poisson's ratios: change in the inelastic Poisson's ratios from cubic to orthotropy is assumed to be the same as the change in the elastic Poisson's ratios. Elastic constants of randomly distributed copper, which are $\mathbb{C}_{11} = \mathbb{C}_{22} = \mathbb{C}_{33}$, $\mathbb{C}_{12} = \mathbb{C}_{13} = \mathbb{C}_{23}$ and $\mathbb{C}_{44} = \mathbb{C}_{55} = \mathbb{C}_{66}$, are obtained from Tome (1998). Three independent engineering

constants, the elastic modulus E, the Poisson's ratio v and the shear modulus μ, are calculated from the elastic constants. Randomly distributed copper has cubic symmetry while rolled copper, which has texture, is orthotropic. The orientation of principal axes of the orthotropic material coincides with the specimen axes. Nine independent elastic constants of orthotropic copper were obtained again from Tome (1998) and are used to determine the nine independent engineering constants which are the three Young's moduli E_{11}, E_{22} and E_{33}, the Poisson's ratios v_{12}, v_{13} and v_{23} and the shear moduli μ_{12}, μ_{13} and μ_{23}. Then percentage changes in the elastic Poisson's ratios from cubic to orthotropy are calculated. Inelastic Poisson's ratios, η_{12}, η_{13} and η_{23}, are determined according to the assumption made above. The rest of the inelastic material constants are determined from the inelastic incompressibility condition ($\mathbb{R}_{iikl} = \mathbb{R}_{klii} = 0$) which leads to six independent equations. Calculated material constants for orthotropic material are given in Table 1.

Fig. 2 shows the axial elongation versus shear strain under free-end torsion for the Jaumann and the logarithmic rate. Simulations are performed at a shear strain rate of $\dot{\gamma} = 1 \times 10^{-3}$ 1/s. The logarithmic rate gives less elongation than the Jaumann rate. Swift (1947) performed the free-end torsion experiments on copper. All experiments on copper were performed on solid bars. It was observed that solid bars yield approximately 3.7% elongation at a shear strain $\gamma = 400\%$, see Fig. 12 of Swift (1947). Thin walled tubular specimens are expected to lead to larger length change than the solid bars. Our simulation with the log-

Table 1
Material constants for fixed anisotropy

Elastic moduli	$E_{11} = 123.13\text{E}3$ MPa
	$E_{22} = 127.86\text{E}3$ MPa
	$E_{33} = 118.9\text{E}3$ MPa
	$\mu_{12} = 22.65\text{E}3$ MPa
	$\mu_{13} = 25.2\text{E}3$ MPa
	$\mu_{23} = 23.9\text{E}3$ MPa
Elastic Poisson's ratios	$v_{12} = 0.316$
	$v_{13} = 0.38$
	$v_{23} = 0.36$
	$E_t = 1000$ MPa
Inelastic moduli	$K_{11} = 1231.3\text{E}3$ MPa
	$K_{22} = 1325.4\text{E}3$ MPa
	$K_{33} = 1173.5\text{E}3$ MPa
	$K_{12} = 427.5\text{E}3$ MPa
	$K_{13} = 376\text{E}3$ MPa
	$K_{23} = 434.17\text{E}3$ MPa
Inelastic Poisson's ratios	$\eta_{12} = 0.44$
	$\eta_{13} = 0.56$
	$\eta_{23} = 0.52$
Isotropic stress	$A_c = 1$
	$A_o = 115$ MPa
	$A_f = 160$ MPa
Viscosity function	$k_1 = 3.142\text{E}5$ s
	$k_2 = 60$ MPa
	$k_3 = 21.98$
Shape function	$C_1 = 3000$ MPa
	$C_2 = 123\,500$ MPa
	$C_3 = 0.11$ MPa^{-1}

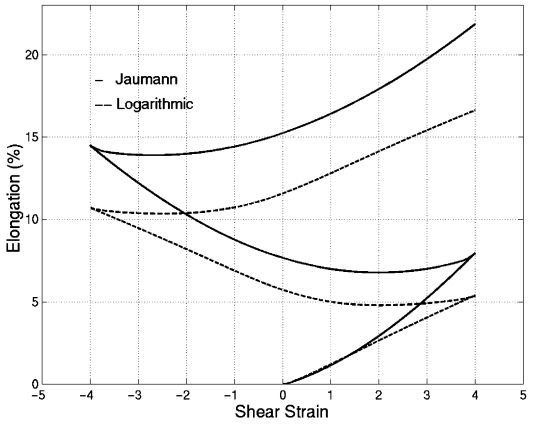

Fig. 2. Axial elongation versus shear strain for orthotropic material (rolled copper) using the Jaumann rate and the logarithmic rate. The material constants are given in Table 1.

arithmic rate yields 5% elongation at shear strain $\gamma = 400\%$. These results are in good agreement with experiments.

2.4. Deformation induced anisotropy

It is well known that the microstructure of materials changes during large deformation. This changes lead to the change of symmetry, initially isotropic materials can be orthotropic at the end of the loading. The change in the material symmetry is accomplished by allowing the change of the inelastic compliance tensor. It is assumed that elastic properties do not change during the deformation.

The behavior of 70:30 brass under free-end torsion is investigated using deformation induced anisotropic finite VBO with the Jaumann and logarithmic rates. Simulations are performed at a shear strain rate of $\dot{\gamma} = 1 \times 10^{-3}$ 1/s. At shear strain $\gamma = 127\%$, the material is unloaded and reloaded until $\gamma = -47\%$. In Fig. 3, axial elongation versus shear strain is plotted for the Jaumann rate. Experimental data is obtained from

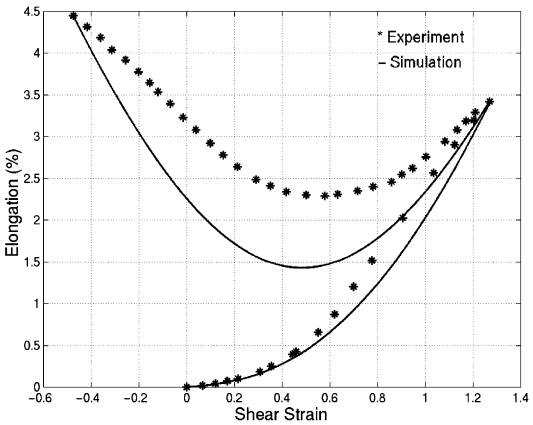

Fig. 3. Axial length change in cyclic free-end torsion by using anisotropic finite VBO with the Jaumann rate. Experimental data are from Swift (1947). Material constants are given in Table 2.

Swift (1947). Material constants are given in Table 2 and used in Figs. 3–7. These material constants are the initial constants when the material is isotropic. The loading curve matches with experimental data quite well. Upon the reversing of loading direction, elongation decreases and reaches a min value, then increases again. Although unloading curve does not match experiment well, the value of elongation at the end of the reloading is the same as in the experiment. Backtracking of shear strain versus elongation curve after unloading is captured well. The corresponding hysteresis loop of 70:30 brass is depicted in Fig. 4. In addition to Cauchy stress, the equilibrium and kinematic stress curves are also plotted.

The experiments made by Billington (1976) on iron showed that work hardening has not much effect on the axial elongation of a tubular or solid bar specimen under free-end torsion. This was a contradiction to

Table 2
Initial isotropic material constants for the modeling of deformation induced anisotropy using anisotropic FVBO

Modulus	$E = 105000$ MPa $E_t = 100$ MPa $K = 105000$ MPa $K_o = 105000$ MPa
The Poisson's ratios	$\eta = 0.5$ $v = 0.3$
Isotropic stress	$A_c = 2$ $A_o = 250$ MPa $A_f = 600$ MPa
Viscosity function	$k_1 = 6.142E5$ s $k_2 = 150$ MPa $k_3 = 12.98$
Shape function	$C_1 = 7000$ MPa $C_2 = 93500$ MPa $C_3 = 0.11$ MPa^{-1}
$b[\bar{e}]$ function	$b[\bar{e}] = 0.51 - 0.508\tanh(2\bar{e})$

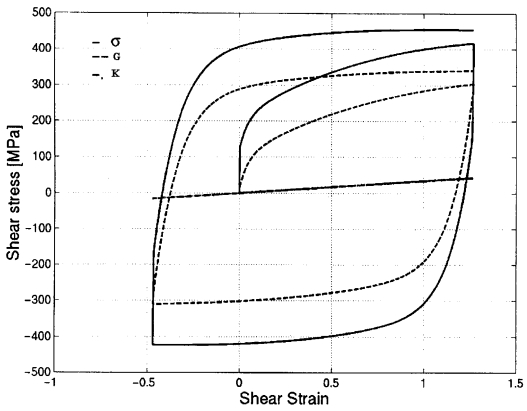

Fig. 4. Hysteresis loop of 70:30 brass under free-end torsion by using anisotropic finite VBO with the Jaumann rate. Initial material constants are given in Table 2.

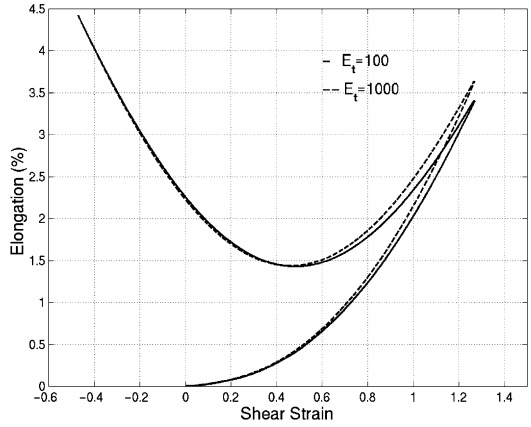

Fig. 5. The effect of monotonic work hardening on axial elongation. The objective rate is the Jaumann rate. Initial material constants are given in Table 2.

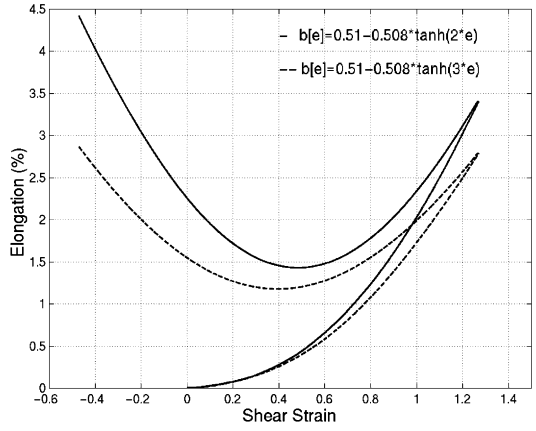

Fig. 6. The effect of $b[\bar{e}]$ function on axial elongation. The objective rate is the Jaumann rate. Initial material constants are given in Table 2.

Swift's statement. In this work, the effects of work hardening are investigated as well. When the tangent modulus is increased by a factor of 10, unloading and reloading curve did not change at all, the axial elongation increased somewhat at loading, see Fig. 5. It can be concluded that the work hardening does not much affect the axial elongation under free-end torsion as Billington (1976) found out experimentally.

The rate of change in anisotropy is controlled by function $b[\bar{e}]$ in the evolution equation of inelastic compliance tensor, $\mathbb{R}$. It is chosen as a positive decreasing function since the rate of the change of anisotropy decreases during deformation, Rollett and Wright (1998). In Fig. 6, the effects of function $b[\bar{e}]$ are shown.

Torsion experiments performed on pure aluminum by Rollett and Wright (1998) have shown the irreversibility of texture development, see their Fig. 8. Torsional load is applied up to 350% shear strain, then unloaded to zero strain. Three sets of pole figures show the initial texture, texture at a shear strain of 350% and at zero strain, Fig. 8a of Rollett and Wright (1998). The relative amount of change in texture that is observed during the deformation from the zero strain condition to 350% strain is considerably greater than

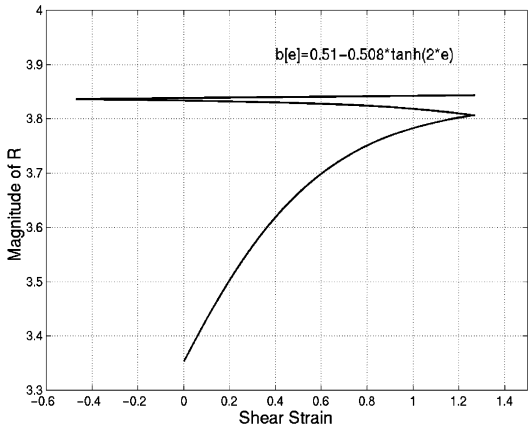

Fig. 7. The magnitude of inelastic compliance tensor versus shear strain. The objective rate is the Jaumann rate. Initial material constants are given in Table 2.

the change that occurs during unloading from 350% strain to zero strain. It is observed that the final texture differs slightly from the texture at a shear strain of 350% and also from the initial state. This implies the irreversibility of texture development. To investigate the irreversibility of texture and the magnitude of changes in anisotropy during deformation, the magnitude of the inelastic compliance tensor is calculated and plotted in Fig. 7. During loading, the change in the magnitude of the inelastic compliance tensor is high, but then slows which is consistent with experimental observations, Rollett and Wright (1998). After unloading, a small change in the magnitude of the inelastic compliance tensor is observed and at the end of a full cycle, the magnitude of the inelastic compliance tensor is found to be somewhat different than at a shear strain of 127%.

For another set of material constants, simulations were performed and axial elongation versus shear strain is depicted in Fig. 8. In this simulation, apart from the material constants given in Table 2, only the viscosity function and $b[\bar{e}]$ function are changed. Used viscosity function constants are $k_1 = 3.142\text{E}6$ s, $k_2 = 240$ MPa and $k_3 = 6.98$ and $b[\bar{e}] = 0.429 - 0.427\tanh(2.3\bar{e})$. By increasing rate dependent effects, almost perfect match in loading and unloading is obtained.

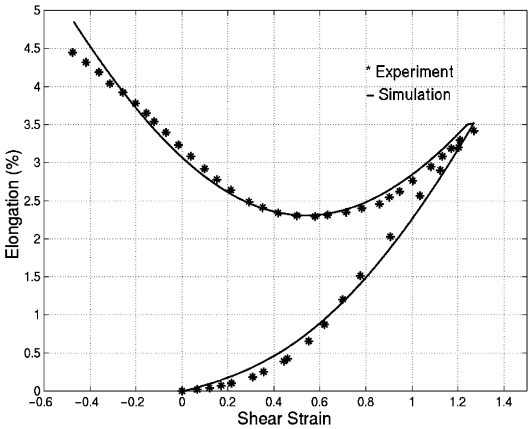

Fig. 8. Axial length change in cyclic free-end torsion by using anisotropic finite VBO with the Jaumann rate.

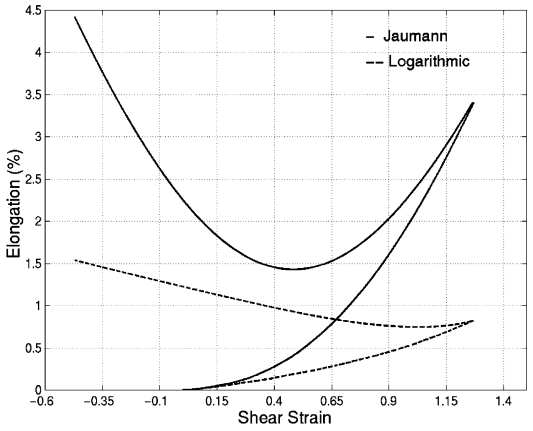

Fig. 9. Axial elongation versus shear strain for two different objective rates, the Jaumann and logarithmic rate. Initial material constants are given in Table 2.

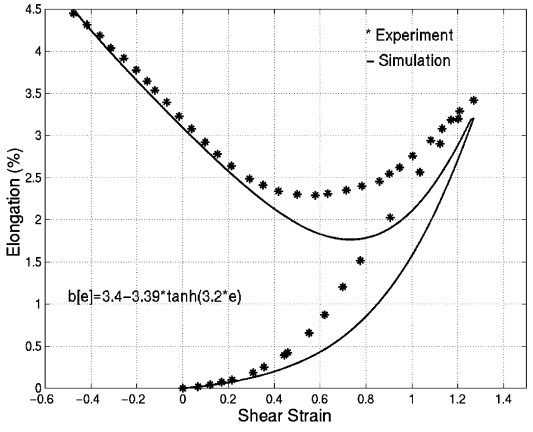

Fig. 10. Axial length change in cyclic free-end torsion. The objective rate is the logarithmic rate. Initial material constants are given in Table 2. Only the function $b[e]$ and the tangent modulus ($E_t = 1000$ MPa) are different from the material constants given in Table 2.

Next simulations are performed with the logarithmic rate. Material constants given in Table 2 are used in these simulations. Axial elongations versus shear strain for two different objective rates, the Jaumann and the logarithmic rates, are depicted in Fig. 9. Logarithmic rate gives less elongation than that of the Jaumann rate. In Fig. 10, the response of the logarithmic rate is given for another set of material constants. All material constants are kept the same as Table 2 except for $b[\bar{e}]$ and E_t. Changes are $b[\bar{e}] = 3.4 - 3.39\tanh(3.2\bar{e})$, and $E_t = 1000$ MPa. A good match with experiment at reloading is obtained with the logarithmic rate.

3. Discussions

The Swift effect is one of the so-called second order phenomena against which the predictive capabilities of constitutive equations are tested. The static, or simply the Swift effect, is found with tubes or solid

cylinders under severe torsion. Under these conditions an axial change in length is found. The first task is then to ascertain whether the model can reproduce the axial strain versus shear number curve, the so-called monotonic Swift effect. Upon reversal of the direction of shearing the curve forms a cusp so that the axial strain reduces before it continues to increase again. The backtracking and the cusp are difficult to model.

The point of discussion is the influence of material symmetry on the modeling of the cyclic Swift effect. Recently, Colak and Krempl (in press) used isotropic FVBO with various objective rates to examine the large strain behavior of a hypothetical alloy close to 70:30 brass under free-end torsion. The limited capability of isotropic formulations to model deformation induced anisotropy is demonstrated through simulations. The unloading behavior for the free-end torsion cannot be reproduced quantitatively when the isotropic formulation of FVBO is used with the appropriate spin. This result is expected, see Majors and Krempl (1994), since the modeling of backtracking of the axial strain versus shear strain curves under free-end torsion requires the repository for deformation induced anisotropy. It cannot be reproduced by formulations using a backstress and appropriate spins alone (e.g. Van der Giessen et al., 1992; Voyiadjis and Kattan, 1992). There appears to exist a consensus that anisotropy is a precondition for observing the Swift effect. Therefore, the monotonic and cyclic Swift effect can be reproduced in this work when an anisotropic model is used.

4. Conclusions

The isotropic finite VBO is extended to anisotropy. It is accomplished by introducing an inelastic compliance tensor and allowing it to evolve with large deformation. The modeling capability of anisotropic VBO was demonstrated for fixed and deformation induced anisotropy. First, the material behavior of rolled copper, which has orthotropic symmetry, is investigated using fixed anisotropic finite VBO. Then, the behavior of the 70:30 brass under free-end torsion is examined using deformation induced anisotropic VBO with the Jaumann and the logarithmic rates. It is shown that monotonic and cyclic Swift effect can be modeled quantitatively by anisotropic finite VBO, which allows the change of inelastic compliance tensor. Change in the material symmetry during large deformation can be observed. Initially isotropic material can become monoclinic or other type of anisotropy.

References

Billington, E.W., 1976. Non-linear mechanical response of various metals: II. Permanent length changes in twisted tubes. J. Phys. D: Appl. Phys. 9, 533–552.

Colak, O.U., Krempl, E., in press. Modeling of the monotonic and cyclic Swift effects using an isotropic, finite viscoplasticity theory based on overstress (FVBO). International Journal of Plasticity.

Krempl, E., 1994. Deformation induced anisotropy. Rensselaer Polytechnic Institute Report Mechanics of Materials Laboratory, 94-3.

Kuroda, M., 1997. Interpretation of the behavior of metals under large plastic shear deformations: a macroscopic approach. International Journal of Plasticity 13 (4), 359–383.

Kuroda, M., 1999. Interpretation of the behavior of metals under large plastic shear deformations: comparison of macroscopic predictions to physically based predictions. International Journal of Plasticity 15, 1217–1236.

Lai, W.M., Rubin, D., Krempl, E., 1993. Introduction to Continuum Mechanics. Pergamon Press.

Lowe, T.C., Lipkin, J., 1991. Analysis of axial deformation response during reverse shear. Journal of the Mechanics and Physics of Solids 39 (3), 417–440.

Majors, P., Krempl, E., 1994. Comments on induced anisotropy, the Swift effect, and finite deformation inelasticity. Mechanics Research Communications 21, 465–472.

Montheillet, F., Gilormini, P., Jonas, J.J., 1985. Relation between axial stresses and texture development during torsion testing: a simplified theory. Acta Metallurgica 33 (4), 705–707.

Rollett, A.D., Wright, S.I., 1998. Typical textures in metals. In: Kocks, U.F., Tome, C.N., Wenk, H.R. (Eds.), Texture and Anisotropy. Cambridge University Press.

Swift, H., 1947. Length changes in metals under torsional overstrain. Engineering 163, 253–257.
Tome, C., 1998. Tensor properties of textured polycrystals. In: Kocks, U.F., Tome, C.N., Wenk, H.R. (Eds.), Texture and Anisotropy. Cambridge University Press.
Van der Giessen, E., Wu, P.D., Neale, K.W., 1992. On the effect of plastic spin on large strain elastic-plastic torsion of solid bars. International Journal of Plasticity 8, 773–801.
Voyiadjis, G., Kattan, P., 1992. Finite elasto–plastic analysis of korsion problems using different spin tensors. International Journal of Plasticity 8, 271–314.
Wu, H., Xu, Z., Wang, P., 1998. Torsion test of aluminum in the large strain range. International Journal of Plasticity 13 (10), 873–892.
Xiao, H., Bruhns, O.T., Meyers, A., 1997. Logarithmic strain, logarithmic spin and logarithmic rate. Acta Mechanica 124, 89–105.
Zidi, M., 2000. Finite torsion and anti-plane shear of a compressible hyperelastic and transversely isotropic tube. International Journal of Engineering Science 38, 1487–1496.